IOP Publishing J. Phys. Mater. 6 (2023) 045001 https://doi.org/10.1088/2515-7639/aceaad

Journal of Physics: Materials

OPEN ACCESS

RECEIVED
30 March 2023

REVISED
27 June 2023

ACCEPTED FOR PUBLICATION
25 July 2023

PUBLISHED
14 August 2023

PAPER

High-harmonic generation in spin and charge current pumping at ferromagnetic or antiferromagnetic resonance in the presence of spin–orbit coupling

Jalil Varela-Manjarres and Branislav K Nikolić*

Department of Physics and Astronomy, University of Delaware, Newark, DE 19716, United States of America
* Author to whom any correspondence should be addressed.

E-mail: bnikolic@udel.edu

Keywords: spintronics, spin pumping, high harmonics, 2D magnetic materials, time-dependent quantum transport, Floquet–Keldysh formalism, spin–orbit coupling

Supplementary material for this article is available online

Abstract

One of the cornerstone effects in spintronics is spin pumping by dynamical magnetization that is steadily precessing (around, for example, the z-axis) with frequency ω_0 due to absorption of low-power microwaves of frequency ω_0 under the resonance conditions and in the absence of any applied bias voltage. The two-decades-old 'standard model' of this effect, based on the scattering theory of adiabatic quantum pumping, predicts that component I^{S_z} of spin current vector $\left(I^{S_x}(t), I^{S_y}(t), I^{S_z}\right) \propto \omega_0$ is time-independent while $I^{S_x}(t)$ and $I^{S_y}(t)$ oscillate harmonically in time with a single frequency ω_0 whereas pumped charge current is zero $I \equiv 0$ in the same adiabatic $\propto \omega_0$ limit. Here we employ more general approaches than the 'standard model', namely the time-dependent nonequilibrium Green's function (NEGF) and the Floquet NEGF, to predict unforeseen features of spin pumping: namely precessing localized magnetic moments within a ferromagnetic metal (FM) or antiferromagnetic metal (AFM), whose conduction electrons are exposed to spin–orbit coupling (SOC) of either intrinsic or proximity origin, will pump both spin $I^{S_\alpha}(t)$ and charge $I(t)$ currents. All four of these functions harmonically oscillate in time at both even and odd integer multiples $N\omega_0$ of the driving frequency ω_0. The cutoff order of such high harmonics increases with SOC strength, reaching $N_{\max} \simeq 11$ in the one-dimensional FM or AFM models chosen for demonstration. A higher cutoff $N_{\max} \simeq 25$ can be achieved in realistic two-dimensional (2D) FM models defined on a honeycomb lattice, and we provide a prescription of how to realize them using 2D magnets and their heterostructures.

1. Introduction

The pumping of electronic spin current by dynamical magnetization of a ferromagnetic metal (FM) into an adjacent normal metal (NM) was originally discovered [1, 2] for steadily precessing magnetization of a FM due to the absorption of low-power (∼mW [3]) microwaves in the ∼GHz range under ferromagnetic (F) resonance conditions. Since it occurs in the absence of any bias voltage, it is termed 'pumping', akin to low-temperature quantum transport where time-dependent quantum systems emit currents [4–6]. Spin pumping has turned out to be a ubiquitous phenomenon in room-temperature spintronic devices, emerging whenever the dynamics of localized magnetic moments is initiated while they interact with conduction electrons to drive them out of equilibrium. For example, recent observations include spin pumping into an adjacent NM from microwave-driven F and ferrimagnetic insulators [7] and antiferromagnetic (AF) insulators [8, 9], as well as from dynamical noncollinear magnetic textures (such as domain walls [10–13], skyrmions [14] and spin waves [15]).

Despite being quintessentially a quantum transport phenomenon, spin pumping is observed even at room temperature because of its interfacial nature [1] where the relevant region around the magnetic

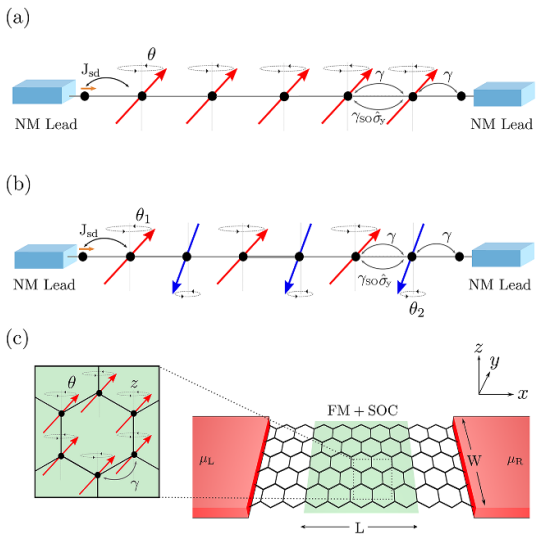

Figure 1. Schematic view of (a), (c) FM- or (b) anti-ferromagnetic metal (AFM)-based setups whose magnetic moments are steadily precessing with frequency ω_0 around the z-axis due to resonant absorption of ∼GHz or ∼THz microwaves, respectively. The setups in (a) and (b) are modeled on a one-dimensional tight-binding lattice attached to two semi-infinite NM leads, while the setup in (c) is modeled on a honeycomb lattice of two-dimensional magnets [35–37] and attached to two semi-infinite graphene nanoribbon leads (SOC, spin–orbit coupling). The precession cone angle is θ in the FM case or $\theta_1 > \theta_2$ for two sublattices in the right-handed mode of precession [8, 17] in the AFM case. In the absence of any bias voltage between macroscopic reservoirs into which NM leads terminate, dynamical magnetic moments interact with conduction electrons via sd exchange coupling J_{sd} to drive them out of equilibrium and pump time-dependent spin $I^{S_\alpha}(t)$ and charge $I(t)$ currents into the NM leads. Electrons hop between the sites with parameter γ, as well as with an additional (equations (1) and (2)) spin-dependent hopping γ_{SO} [39], describing the Rashba SOC [34] within the FM or AFM central region.

material/NM interface is always thinner [16] than the decoherence lengths for electronic orbital and spin degrees of freedom. Thus, the 'standard model' [1] of spin pumping is built using the scattering theory [5] of quantum transport to describe how magnetization of ferromagnets, or both the Néel vector and nonequilibrium magnetization of antiferromagnets [8, 9, 17], precessing with frequency ω_0 around the easy (z-axis) pushes electrons out of equilibrium. The ensuing flowing electronic spins comprise a spin current vector $\left(I^{S_x}(t), I^{S_y}(t), I^{S_z}\right)$ whose I^{S_z} component is time-independent while $I^{S_x}(t)$ and $I^{S_y}(t)$ oscillate harmonically in time at a single frequency ω_0 [1]. These DC and AC components of the pumped spin current can be converted into DC [18] and AC [19] voltages, respectively, by the inverse spin Hall effect and then measured using standard electrical circuits [2]. The magnitude of each component is $\propto \omega_0$, as the signature of general adiabatic quantum pumping [4–6], as well as $\propto \sin^2\theta$ [1, 16] when the precession cone angle θ is controlled by the input microwave power [3, 20]. The spin pumping effectively generates additional dissipation [1, 10, 13] for the magnetization dynamics, so that such loss of spin angular momentum can be employed for indirect [1, 2, 11] detection of pumping.

Thus, the 'standard model' of spin pumping excludes the possibility of higher harmonics in periodic time dependence of any of the three components of the thus generated spin current. Alternatives to the 'standard model' include the Floquet nonequilibrium Green's function (Floquet NEGF) [21–25] or the Kubo formalism [26], developed in order to include possibly strong spin–orbit coupling (SOC) directly at the F(AF) material/NM interface where the analytical formula of the 'standard model' ceases to be applicable [1, 21, 23, 27]. However, these alternatives have focused on computing the time-averaged (i.e. DC) component of pumped spin or charge currents, $I^{S_\alpha,\mathrm{DC}} = \frac{1}{\tau}\int_0^\tau \mathrm{d}t I^{S_\alpha}(t)$ or $I^{\mathrm{DC}} = \frac{1}{\tau}\int_0^\tau \mathrm{d}t I(t)$, where $\tau = 2\pi/\omega_0$ is the period, so possible high harmonics in periodic time dependence of $I^{S_\alpha}(t)$ ($\alpha \in \{x,y,z\}$) or $I(t)$ are overlooked by them as well. The same focus on the DC component of current appears in studies of pumping from nonmagnetic systems [28]. Extending scattering [29] or Floquet NEGF [30] formalisms to obtain complete periodic time dependence, $I^{S_\alpha}(t) = I^{S_\alpha}(t+\tau)$ and $I(t) = I(t+\tau)$, can detect integer high harmonics but would miss the possibility of non-integer [31] harmonics (or interharmonics in the engineering literature [32]).

In this paper we examine two-terminal (one-dimensional, 1D) setups illustrated in figures 1(a) and (b) via the time-dependent NEGF (TDNEGF) formalism [33]. In addition, we examine a two-terminal two-dimensional (2D) setup in figure 1(c) via the time-independent Floquet NEGF [21, 29]. The TDNEGF formalism is more general than the commonly used scattering approach to spin pumping [1, 17] or the Floquet NEGF formalism as it can yield both transient and (at longer times) time-periodic (or nonperiodic when magnetic moments are not steadily precessing [12, 13]) pumped spin and charge currents in a

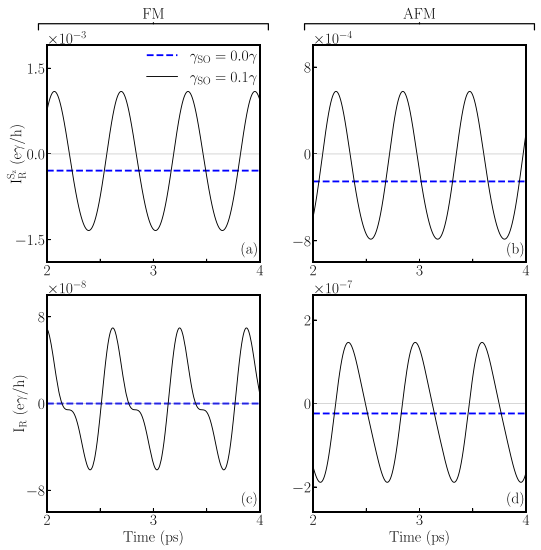

Figure 2. Time-dependent NEGF-computed time dependence of (a), (b) spin $I_R^{S_z}(t)$ and (c), (d) charge $I_R(t)$ currents, after the transient response has died out, pumped into the right NM lead in (a), (c) a FM setup or (b), (d) an AFM setup. The Rashba SOC (equation (1)) is turned off ($\gamma_{SO} = 0$) or turned on ($\gamma_{SO} = 0.1\gamma = J_{sd}$) within the entire magnetic central region in figure 1.

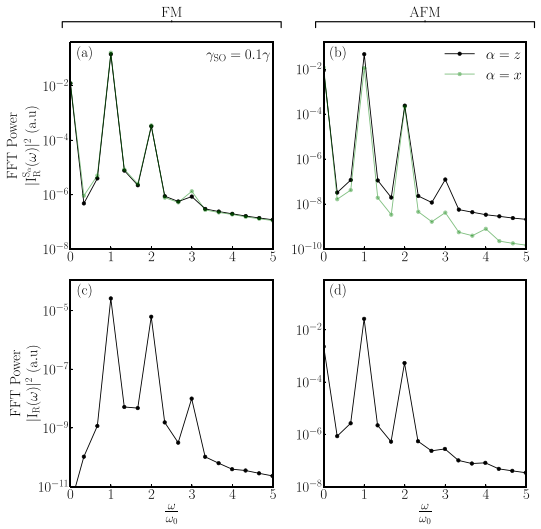

Figure 3. (a)–(d) FFT power spectrum of TDNEGF-computed pumped spin $|I_R^{S_z}(\omega)|^2$ and charge $|I_R(\omega)|^2$ currents from figures 2(a)–(d), respectively. Panels (a) and (b) also show the FFT power spectrum of pumped spin current $|I_R^{S_x}(\omega)|^2$.

numerically exact fashion. However, it is also more expensive computationally and not really necessary if only integer harmonics are confirmed in time-periodic currents in the long time limit. In figure 1(a) a FM and in figure 1(b) an antiferromagnetic metal (AFM), host both magnetic moments and conduction electrons subject to the Rashba type of SOC [34] throughout the whole magnetic region. These FM or AFM regions are sandwiched between two semi-infinite NM leads terminating in macroscopic reservoirs kept at the same chemical potential $\mu_L = \mu_R = E_F = 0$ (so, lattices in figure 1 are half filled by electrons) and temperature $T = 300$ K [38]. In figure 1(c), we assume that the 2D FM region—typically defined on a honeycomb lattice and hosting strong SOC [35–37], chosen here to be also of the Rashba type—is sandwiched between two semi-infinite graphene leads. Starting from an equilibrium state described by the grand canonical density matrix (see equation (4) in [12]), all magnetic moments modeled as classical vectors $\mathbf{M}_i$ of unit length start to precess uniformly at time $t = 0$ around the z-axis with frequency ω_0 and precession cone angle θ in the case of FMs in figures 1(a) and (c) or with precession cone angles θ_1 and θ_2 for magnetic moments $\mathbf{M}_i$ on sublattice A and $\mathbf{M}_{i+1}$ on sublattice B of an AFM.

Our principal results in figures 2–5 for pumping at F or AF resonance show that, once Rashba SOC is turned on, $I^{S_z}(t)$ becomes time dependent (figures 2(a) and (b)) and pumping of nonzero charge current $I(t)$ (figures 2(c) and (d)) occurs as well. Both spin and charge currents exhibit high harmonics in their fast Fourier transform (FFT) power spectrum (figure 3) at both even and odd integer multiples $N\omega_0$ of the

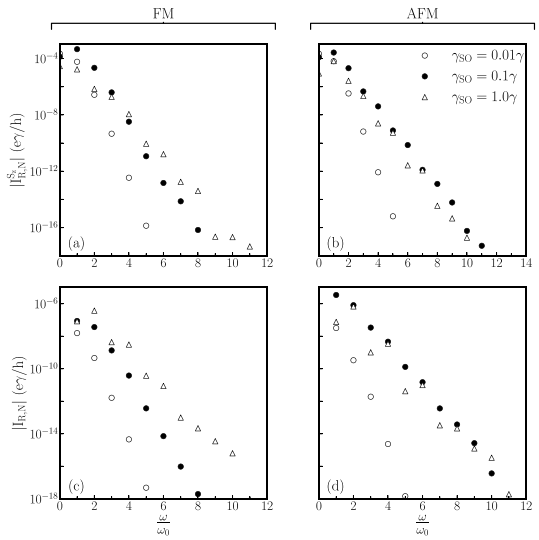

Figure 4. (a)–(d) High harmonics of Floquet NEGF-computed (equation (11)) pumped spin $|I^{S_z}_{R,N}|$ and charge $|I_{R,N}|$ currents for the same 1D FM and AFM systems studied in figures 2(a)–(d), respectively, for three different values of the Rashba SOC (equation (1)) γ_{SO}.

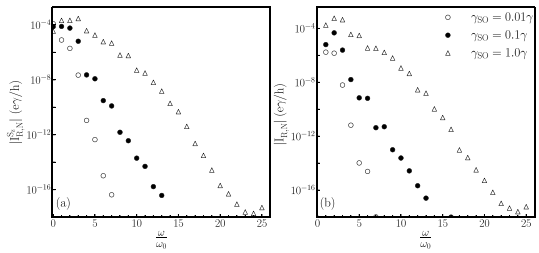

Figure 5. (a)–(d) High harmonics of Floquet NEGF-computed (equation (11)) pumped spin (a) $|I^{S_z}_{R,N}|$ and (b) charge $|I_{R,N}|$ currents for a 2D FM system on the honeycomb lattice (figure 1(c)) for three different values of the Rashba SOC (equation (2)) γ_{SO}.

driving frequency ω_0, whose cutoff $N_{\max}$ can be controlled by the strength of the SOC (figures 4 and 5). In particular, using a 2D FM cutoff can reach $N_{\max} \simeq 25$. Prior to delving into these results, we introduce useful concepts and notation.

2. Models and methods

The electronic system within the FM region in figure 1(a) or the AFM region in figure 1(b) is modeled by a 1D tight-binding (TB) Hamiltonian

$$\hat{H}_{1D}(t) = -\gamma \sum_{\langle ij \rangle} \hat{c}_i^\dagger \hat{c}_j - J_{sd} \sum_i \hat{c}_i^\dagger \hat{\boldsymbol{\sigma}} \cdot \mathbf{M}_i(t) \hat{c}_i - \mathrm{i}\gamma_{SO} \sum_{\langle ij \rangle} \hat{c}_i^\dagger \hat{\sigma}_y \hat{c}_j, \tag{1}$$

where $\hat{c}_i^\dagger = (\hat{c}_{i\uparrow}^\dagger \;\; \hat{c}_{i\downarrow}^\dagger)$ is a row vector containing operators $\hat{c}_{i\sigma}^\dagger$ which create an electron with spin $\sigma = \uparrow, \downarrow$ at site i, $\hat{c}_i$ is a column vector containing the corresponding annihilation operators, γ is the hopping between the nearest-neighbor (NN) sites (signified by $\langle \ldots \rangle$), also setting the unit of energy, γ_{SO} is an additional spin-dependent hopping [39] due to the Rashba SOC [34] and the conduction electron spin, described by the vector of the Pauli matrices $\hat{\boldsymbol{\sigma}} = (\hat{\sigma}_x, \hat{\sigma}_y, \hat{\sigma}_z)$, interacts with the classical magnetic moments $\mathbf{M}_i(t)$ via sd exchange interaction of strength $J_{sd} = 0.1\gamma$ [40]. We use $N_{\text{sites}} = 9$ ($N_{\text{sites}} = 10$) sites in the FM (AFM) central region, ensuring maximum outflowing spin current (which in one dimension oscillates as a function of N_{sites} [12]). The left (L) and the right (R) NM leads, sandwiching the FM or AFM region in figure 1, are semi-infinite 1D TB chains described by the first term alone in equation (1). The Fermi energy of the macroscopic reservoirs into which the NM leads terminate is $E_F = 0$.

Similarly, the electronic system within the FM region in figure 1(c) is modeled by a 2D TB Hamiltonian defined on the honeycomb lattice

$$\hat{H}_{\rm 2D}(t) = -\gamma \sum_{\langle ij \rangle} \hat{c}_i^\dagger \hat{c}_j - J_{sd} \sum_i \hat{c}_i^\dagger \hat{\boldsymbol{\sigma}} \cdot \mathbf{M}(t) \hat{c}_i + \mathrm{i}\gamma_{\rm SO} \sum_{\langle ij \rangle} \hat{c}_i^\dagger \left(\hat{\boldsymbol{\sigma}} \times \mathbf{d}_{ij} \right) \cdot \mathbf{e}_z \hat{c}_j, \tag{2}$$

where $\mathbf{d}_{ij}$ is the vector connecting NN sites i and j, $\gamma_{\rm SO}$ is the strength of the Rashba SOC and $\mathbf{e}_z$ is the unit vector along the z-axis. The L and R leads in figure 1(c) are semi-infinite graphene nanoribbons (GNRs) with zigzag edges described by the first term alone in equation (2). In equation (2), we use the same hopping γ in the FM region and in the GNR leads, while $J_{sd} = 0.1\gamma$ in the FM region only. The size of the FM region is $4.5\sqrt{a} \times 8a$, with a being the distance between NN sites. The Fermi energy of the macroscopic reservoirs into which the GNR leads terminate is $E_{\rm F} = 0$.

In the FM cases (figures 1(a) and (c)), all magnetic moments precess uniformly with the same frequency ω_0 and the cone angle $\theta = 20^\circ$ (which is near the maximum that can be achieved in practice without introducing nonlinearities [3, 20]). This means that $\mathbf{M}_i(t) = \left(\sin\theta\cos(\omega_0 t), \sin\theta\sin(\omega_0 t), \cos\theta\right)$ is plugged into equation (1). On the other hand, at AF resonance two precession modes of sublattice magnetic moments are possible, with left-handed and right-handed (RH) chiralities [17], where both $\mathbf{M}_i^{\rm A}(t)$ and $\mathbf{M}_i^{\rm B}(t)$ undergo a clockwise or counterclockwise precession with π phase difference, respectively. Thus, in the case of the AFM central region (figure 1(b)) we use the RH mode, $\mathbf{M}_i(t) = \left(\sin\theta\cos(\omega_0 t), \sin\theta\sin(\omega_0 t), \cos\theta\right)$ and $\mathbf{M}_{i+1}(t) = \left(\sin\theta\cos(\omega_0 t + \pi), \sin\theta\sin(\omega_0 t + \pi), \cos\theta\right)$, with $\theta_1 = 20^\circ$ and the ratio $\theta_1/\theta_2 = 1.29$ fixed to correspond to the RH mode of MnF_2 employed in recent experiments [8]. We use the same driving frequency $\hbar\omega_0 = 0.01\gamma$ for both FM and AFM 1D cases, which is realistic for the latter but too large for the former. This reduces the computational expense of TDNEGF calculations, while not affecting the result since the magnitude of all pumped currents scales linearly with ω_0 (so the results for the FM case are easily rescaled to realistic frequencies). For calculations of the 2D FM case (figure 1(c)) via the Floquet NEGF formalism the choice of frequency is not important computationally as long as $\hbar\omega \ll E_{\rm F}$, so that the expression for harmonics of the pumped current can be simplified to equation (11) that does not require integration [29] over energy.

The fundamental quantity of quantum statistical mechanics is the density matrix. The time-dependent one-particle nonequilibrium density matrix can be expressed [33] by $\boldsymbol{\rho}^{\rm neq}(t) = \hbar\mathbf{G}^<(t,t)/i$ in terms of the lesser Green's function of the TDNEGF formalism defined by $G_{ii'}^{<,\sigma\sigma'}(t,t') = \frac{i}{\hbar}\langle \hat{c}_{i'\sigma'}^\dagger(t') \hat{c}_{i\sigma}(t) \rangle_{\rm nes}$ where $\langle \ldots \rangle_{\rm nes}$ is the nonequilibrium statistical average [41]. We solve a matrix integro-differential equation [12, 38]

$$\mathrm{i}\hbar \frac{\mathrm{d}\boldsymbol{\rho}^{\rm neq}}{\mathrm{d}t} = [\mathbf{H}(t), \boldsymbol{\rho}^{\rm neq}] + \mathrm{i} \sum_{p=L,R} [\boldsymbol{\Pi}_p(t) + \boldsymbol{\Pi}_p^\dagger(t)] \tag{3}$$

for the time evolution of $\boldsymbol{\rho}^{\rm neq}(t)$, where $\mathbf{H}(t)$ is the matrix representation of the Hamiltonian in equation (1). Equation (3) is an exact quantum master equation for the reduced density matrix of the central FM or AFM region viewed as an open finite-size quantum system attached to macroscopic Fermi liquid reservoirs via semi-infinite NM leads. The $\boldsymbol{\Pi}_p(t)$ matrices

$$\boldsymbol{\Pi}_p(t) = \int_{t_0}^{t} \mathrm{d}t_2 \left[\mathbf{G}^>(t,t_2)\boldsymbol{\Sigma}_p^<(t_2,t) - \mathbf{G}^<(t,t_2)\boldsymbol{\Sigma}_p^>(t_2,t) \right] \tag{4}$$

are expressed in terms of the lesser and greater Green's functions [41] and the corresponding self-energies $\boldsymbol{\Sigma}_p^{>,<}(t,t')$ [38]. They yield the directly time-dependent charge current, $I_p(t) = \frac{e}{\hbar}\mathrm{Tr}\left[\boldsymbol{\Pi}_p(t)\right]$, and spin current, $I_p^{S_\alpha}(t) = \frac{e}{\hbar}\mathrm{Tr}\left[\hat{\sigma}_\alpha \boldsymbol{\Pi}_p(t)\right]$, pumped into the lead $p = L, R$. We use the same units for charge and spin currents, defined as $I_p = I_p^\uparrow + I_p^\downarrow$ and $I_p^{S_\alpha} = I_p^\uparrow - I_p^\downarrow$, in terms of spin-resolved charge currents I_p^σ. In our convention a positive current in the NM lead p means charge or spin is flowing *out* of that lead.

Although we use a 1D TB chain to model FM and AFM setups in figure 1, these setups can be easily converted into three-dimensional (3D) realistic junctions with a macroscopic cross section by assuming that the chain is disorder-free and periodically repeated in the y- and z-directions. This means that our TDNEGF calculations would have to be repeated at each (k_y, k_z) point [16]. Nevertheless, by studying simpler 1D models we can capture essential features of pumping from realistic 3D systems (e.g. compare figure 3 for a 3D junction with realistic atomistic structure to figure 4 for a 1D junction described by the simplistic TB model in [24]).

In addition to TDNEGF calculations, we also employ the Floquet NEGF approach, operating with time-independent quantities (equations (5)–(12)), which is far less computationally demanding and can also be used to validate (figure 4) TDNEGF calculations once it is confirmed (figure 3) that only integer

harmonics are present in the pumped currents. The Floquet theorem is usually discussed [42–44] as specifying the form of the solution of the time-dependent Schrödinger equation, $i\hbar\partial|\psi(t)\rangle/\partial t = \hat{H}(t)|\psi(t)\rangle$, for a Hamiltonian periodic in time $\hat{H}(t+\tau) = \hat{H}(t)$. That is, an arbitrary solution $|\psi(t)\rangle = \sum_\eta c_\eta e^{-i\varepsilon_\eta(t-t_0)}|u_\eta(t)\rangle$ can be expanded in terms of Floquet states $|\phi_\eta(t)\rangle = e^{-i\varepsilon_\eta t/\hbar}|u_\eta(t)\rangle$ with periodic $|u_\eta(t+\tau)\rangle = |u_\eta(t)\rangle$, quasienergy $\varepsilon_\eta \in \mathbb{R}$ and $c_\eta = \langle u_\eta(t_0)|\psi(t_0)\rangle$. The same Floquet theorem can be restated for double Fourier transformed (i.e. from t, t' to E, E' variables) NEGFs

$$\mathbf{G}^{r,<}(t,t') = \int_{-\infty}^{+\infty}\frac{dE}{2\pi}\int_{-\infty}^{+\infty}\frac{dE'}{2\pi}\, e^{-iEt/\hbar + iE't'/\hbar}\mathbf{G}^{r,<}(E,E'), \tag{5}$$

as the requirement that energies E, E' are not independent (as would be the case in the general situation where the Hamiltonian is not time-periodic) but instead satisfy

$$\mathbf{G}^{r,<}(E,E') = \mathbf{G}^{r,<}(E,E+n\hbar\omega_0) = \mathbf{G}^{r,<}_n(E). \tag{6}$$

The coupling of energies E and $E+n\hbar\omega_0$ (n is an integer) indicates 'multiphoton' exchange processes. In the absence of many-body (electron–electron or electron–boson) interactions, currents can be expressed using solely [21, 45] the Floquet-retarded GF $\check{\mathbf{G}}^r(E)$

$$[E + \check{\mathbf{\Omega}} - \check{\mathbf{H}}_F - \check{\mathbf{\Sigma}}^r(E)]\check{\mathbf{G}}^r(E) = \check{1}, \tag{7}$$

which is composed of $\mathbf{G}^r_n(E)$ submatrices along the diagonal. Here

$$\check{\mathbf{H}}_F = \begin{pmatrix} \ddots & \vdots & \vdots & \vdots & \iddots \\ \cdots & \mathbf{H}_0 & \mathbf{H}_1 & \mathbf{H}_2 & \cdots \\ \cdots & \mathbf{H}_{-1} & \mathbf{H}_0 & \mathbf{H}_1 & \cdots \\ \cdots & \mathbf{H}_{-2} & \mathbf{H}_{-1} & \mathbf{H}_0 & \cdots \\ \iddots & \vdots & \vdots & \vdots & \ddots \end{pmatrix} \tag{8}$$

is a time-independent but infinite matrix representation of the so-called Floquet Hamiltonian [42–44] whose finite submatrices $\mathbf{H}_n$ of size $N_{\text{sites}} \times N_{\text{sites}}$ are matrix representations (in the basis of orbitals $|i\rangle$) of the coefficients $\hat{H}_n$ in the Fourier expansion $\hat{H}(t) = \sum_{n=-\infty}^{\infty} e^{-in\omega_0 t}\hat{H}_n$. In addition, in equation (7) we use the following notation

$$\check{\mathbf{\Omega}} = \begin{pmatrix} \ddots & \vdots & \vdots & \vdots & \iddots \\ \cdots & -\hbar\omega_0 1 & 0 & 0 & \cdots \\ \cdots & 0 & 0 & 0 & \cdots \\ \cdots & 0 & 0 & \hbar\omega_0 1 & \cdots \\ \iddots & \vdots & \vdots & \vdots & \ddots \end{pmatrix} \tag{9}$$

and $\check{\mathbf{\Sigma}}^r(E)$ is the retarded Floquet self-energy matrix

$$\check{\mathbf{\Sigma}}^r(E) = \begin{pmatrix} \ddots & \vdots & \vdots & \vdots & \iddots \\ \cdots & \mathbf{\Sigma}^r(E-\hbar\omega_0) & 0 & 0 & \cdots \\ \cdots & 0 & \mathbf{\Sigma}^r(E) & 0 & \cdots \\ \cdots & 0 & 0 & \mathbf{\Sigma}^r(E+\hbar\omega_0) & \cdots \\ \iddots & \vdots & \vdots & \vdots & \ddots \end{pmatrix} \tag{10}$$

composed of the usual self-energies of the leads [46], $\mathbf{\Sigma}^r(E) = \sum_{p=L,R}\mathbf{\Sigma}^r_p(E)$, on the diagonal. All matrices labeled as $\check{\mathbf{O}}$ are representations of operators acting in the so-called Floquet–Sambe [43] space, $\mathcal{H}_F = \mathcal{H}_\tau \otimes \mathcal{H}_e$, where $\mathcal{H}_e$ is the Hilbert space of electronic states spanned by localized orbitals $|i\rangle$ and $\mathcal{H}_\tau$ is the Hilbert space of periodic functions with period $\tau = 2\pi/\omega_0$ spanned by orthonormal Fourier vectors $\langle t|n\rangle = \exp(in\omega_0 t)$. Note that $\mathbf{1}$ is the unit matrix in $\mathcal{H}_e$ space and $\check{1}$ is the unit matrix in $\mathcal{H}_F = \mathcal{H}_\tau \otimes \mathcal{H}_e$ space.

The scattering matrix [1] of the Landauer–Büttiker approach to quantum transport, generalized to time-periodic multi-terminal devices [28, 29], makes it possible to express the Nth harmonic of spin current flowing into lead p as [29]

$$I^{S_\alpha}_{p,N} = \frac{e}{h}\hbar\omega_0 \sum_{p'=L,R}\sum_{n=-\infty}^{\infty} n\mathrm{Tr}\left[\hat{\sigma}_\alpha \mathbf{S}^\dagger_{pp'}\left(E_\mathrm{F}+n\hbar\omega_0, E_\mathrm{F}\right)\mathbf{S}_{pp'}\left(E_\mathrm{F}+(n+N)\hbar\omega_0, E_\mathrm{F}\right)\right]. \tag{11}$$

Equation (11) is written in the limit of zero temperature and small frequency $\hbar\omega_0 \to 0$, which removes integrals [29] over energy and sets all quantities to depend only on the Fermi energy E_F. The charge current in lead p is obtained from the same equation (11) by the replacement $\hat{\sigma}_\alpha \mapsto \hat{\sigma}_0$, where $\hat{\sigma}_0$ is the unit 2×2 matrix. Note that $I^{S_z}_{p,0}$ ($I_{p,0}$) is the DC component of spin (charge) current, respectively. The Floquet scattering matrix [28, 29] $\mathbf{S}_{pp'}(E_\mathrm{F}+n\hbar\omega_0, E_\mathrm{F})$ describes quantum transport of electrons at the Fermi energy from lead p' to p while they absorb or emit $n\hbar\omega_0$ 'photons'. We compute $\mathbf{S}_{pp'}(E_\mathrm{F}+n\hbar\omega_0, E_\mathrm{F})$ by using the generalization [28, 47, 48] of the Fisher–Lee formula, originally derived for steady-state quantum transport [49], to the case of periodically driven multi-terminal devices

$$\mathbf{S}_{pp'}(E_\mathrm{F}+n\hbar\omega_0, E_\mathrm{F}) = \delta_{pp'}\delta_{E_\mathrm{F}+n\hbar\omega_0,E_\mathrm{F}} - \mathrm{i}\sqrt{\mathbf{\Gamma}_p(E_\mathrm{F}+n\hbar\omega_0)}\mathbf{G}^r_{pp'}(E_\mathrm{F}+n\hbar\omega_0, E_\mathrm{F})\sqrt{\mathbf{\Gamma}_{p'}(E_\mathrm{F})}. \tag{12}$$

Here $\mathbf{G}^r_{pp'}(E_\mathrm{F}+n\hbar\omega_0, E_\mathrm{F})$ is the submatrix of the Floquet retarded GF $\check{\mathbf{G}}^r(E)$ (equation (7)), whose matrix elements connect sites along the edges of the central region that are also connected (via nonzero hopping) to the sites of the leads p and p', and $\mathbf{\Gamma}_p(E) = \mathrm{i}[\mathbf{\Sigma}^r_p(E) - \mathbf{\Sigma}^r_p(E)^\dagger]$ is the level-broadening matrix [33, 38, 41, 46] of lead p. By truncating the infinite-dimensional space $\mathcal{H}_\tau$ to dimension $|n| \leqslant n_\mathrm{max}$ we also convert infinite matrices $\check{\mathbf{O}}$ to finite-size ones suitable for numerical calculations, where convergence in n is achieved by ensuring that each Nth harmonic of pumped current in lead p satisfies $|(I_{p,N}(n_\mathrm{max}) - I_{p,N}(n_\mathrm{max}-1)/I_{p,N}(n_\mathrm{max}-1)| < \delta$ with $\delta = 10^{-2}$ chosen. This typically requires the use of $n_\mathrm{max} \leqslant 6$ for all harmonics N.

3. Results and discussion

We warm up with calculations (flat dashed lines in figure 2) reproducing 'standard model' results for spin pumping from a FM [1] or AFM [17] in the absence of SOC, $\gamma_\mathrm{SO} = 0$. As expected, our TDNEGF calculations reproduce time-independent $I^{S_z}_p$ and $I_p = 0$ (in the FM case) at sufficiently long times, after the transient response has died out. The emergence of $I^{S_z}_p$ and $I_p \neq 0$ (in the AFM case) can be understood from the rotating frame picture of spin pumping [16, 50–53] where time-dependent setups in figure 1 are mapped, by a unitary transformation into the frame that rotates with magnetization onto four-terminal time-independent ones with effective bias voltage $\hbar\omega_0/e$ [16, 51, 52] between the left or the right pair of leads. In the rotating frame, $I^{S_z}_p$ is time-independent and it remains so upon transforming it into the lab frame, while $I_p = 0$ in symmetric FM devices. The general requirement for the appearance of a nonzero DC component of pumped charge current—that the left–right symmetry of a two-terminal device must be broken [6, 48, 54]—helps to validate the correctness of the TDNEGF calculations. If this is done by breaking both inversion symmetry and time-reversal symmetry dynamically (such as by two spatially separated potentials oscillating out-of-phase [4–6]) then the DC component of charge current is nonzero and $\propto \omega_0$ at (sufficiently low) driving frequencies. If only one of these two symmetries is broken, and this does not have to occur dynamically, then the DC component of pumped current is $\propto \omega_0^2$ as the signature of nonadiabatic charge pumping [6, 16, 48, 54]. Since the FM setup in figure 1(a) is left–right symmetric, the DC component of pumped charge current in the presence of SOC is zero in figure 2(c). Conversely, the AFM setup in figure 1(b) has broken (by configuration of magnetic moments) left–right symmetry, so the DC component of its pumped charge current is nonzero in figure 2(d).

The rotating frame description becomes inapplicable when time-independent SOC is turned on in the lab frame because SOC becomes time-dependent in the rotating frame. Therefore, we switch to TDNEGF calculations in figure 2 revealing that, as soon as the Rashba SOC is turned on, $I^{S_z}_p(t)$ oscillates harmonically and nonzero time-periodic $I_p(t)$ is also established. Note that DC or perfectly harmonic currents are ensured in the long time limit by a continuous energy spectrum of setups in figure 1 brought by the attached NM leads and, thereby, dissipation effects generated by fermionic reservoirs.

Figure 3 shows that upon turning the Rashba SOC on, the FFT power spectrum of pumped spin (note that spectra of $|I^{S_z}_R(\omega)|^2$ and $|I^{S_x}_R(\omega)|^2$ are nearly identical) and charge currents will also contain high harmonics at frequencies $n = \omega/\omega_0$ for both even and odd integer N. Since only integer harmonics are present, in figure 4 we switch to the Floquet NEGF formalism to show $|I_{R,N}|$ and $|I^{S_z}_{R,N}|$ versus harmonic order N. This allows us to determine the cutoff harmonic order $N_\mathrm{max} \simeq 11$ with increasing SOC more precisely

than when using TDNEGF calculations and FFT of their results (where apparently $N_{\max} \simeq 4$ in figure 3) where numerical artifacts are easily introduced by the choice of time step and FFT window.

The microscopic origin of the transition from time-independent $I_p^{S_z}$ for $\gamma_{SO} = 0$ to time-dependent $I_p^{S_z}(t)$ for $\gamma_{SO} \neq 0$ can be understood from an animation, provided as supplementary data[1], of nonequilibrium spin density $\langle \hat{\mathbf{s}}_1 \rangle^{\text{neq}}(t) = \text{Tr}\left[|1\rangle\langle 1| \otimes \hat{\boldsymbol{\sigma}} \boldsymbol{\rho}^{\text{neq}}(t)\right]$ at site 1 in the FM case. While $\langle \hat{s}_i^z \rangle^{\text{neq}}$ is time-independent for $\gamma_{SO} = 0$ [1, 55], it becomes harmonically time dependent with frequency ω_0 and its integer multiples, so that $\langle \hat{\mathbf{s}}_i \rangle^{\text{neq}}(t)$ nutates as it flows out of FM to comprise [55] a pumped spin current and give rise to $I_p^{S_z}(t)$.

The predicted high-harmonic spectra (figure 4) for spin and charge currents pumped by precessing magnetization bear resemblance to a field where high-harmonic generation in pumped charge current has been intensely pursued in recent years—solids driven out of equilibrium by laser light of frequency ω_0 [56]. For example, inversion symmetric bulk semiconductors driven by strong mid-infrared laser light, whose $\hbar\omega_0$ is much smaller than the band gap, can exhibit a nonlinear effect generating new radiation at odd multiples of ω_0 [56]. Furthermore, in 2D systems breaking inversion symmetry, such as monolayers of MoS_2 [56] or surface states of topological materials [57], additional even-order harmonics or non-integer harmonics [57] can emerge. This has inspired recent theoretical studies on possible high-harmonic generation in spin currents pumped by laser light irradiating magnetic insulators [58, 59] as well as in spin–orbit-split 3D materials [60] and 2D electron gases [61]. However, these schemes rely on highly nonlinear effects in strong light–matter coupling, and in the case of magnetic insulators they assume coupling of the magnetic field of laser light directly to localized magnetic moments. Since such coupling is $1/c$ times smaller than light–charge coupling, they would require intense THz laser pulses beyond currently available technologies.

On the other hand, setups in figure 1 are routinely made in spintronics using widely available microwave sources and, in contrast to optical pumping, with low input power (∼mW) [3] and the possibility for scalability. For example, first-principles Floquet NEGF analysis [24] of the very recent experiments [8] on spin pumping from the AF insulator MnF_2 in contact with heavy metal Pt has revealed that the MnF_2 layer can be significantly modified by the spin–orbit proximity effect [23, 24, 62–65] within such heterostructures due to SOC at interfaces or from the bulk of the Pt layer. This means that re-examination of such experiments, where all key ingredients for our predictions are already present, could reveal high harmonics in electromagnetic radiation produced by pumped time-dependent charge current (figures 2(d) and 3(d)) or spin current (figures 2(b) and 3(b)) converted to charge current [19] by the Pt layer.

Furthermore, one could search for F or AF materials with strong intrinsic SOC [66]. In this respect, 2D magnetic materials [35] are a particularly promising choice since their magnetic ordering at finite temperature crucially relies on magnetic anisotropy originating from strong SOC [36, 37]. In addition, 2D magnetic materials can be easily spin–orbit proximitized [62] by transition metal dichalcogenides to further tune their properties [65]. Thus, taking into account that 2D magnetic materials are typically of a honeycomb or hexagonal lattice type [35–37], we examine a 2D setup in figure 1(c) where the honeycomb lattice hosting both precessing magnetic moments and Rashba SOC (equation (2)) is attached to semi-infinite GNR leads. The pumped spin (figure 5(a)) and charge (figure 5(b)) currents in such a model of a 2D magnet at F resonance exhibit high harmonics with a larger cutoff $N_{\max} \simeq 25$ than in the case of the 1D setups studied in figure 4. Note that by replacing the honeycomb lattice in figure 1(c) with a square lattice we obtain $N_{\max} \simeq 12$.

4. Conclusions

Using TDNEGF calculations [33, 38], applicable to arbitrary time-dependent quantum transport of spin and charge in multi-terminal devices [6, 12, 13], we find that, when periodically driven by microwaves, magnetic moments of FM or AFM materials will pump spin and charge currents oscillating at both the frequency ω_0 of the driving field and its integer high harmonics $N\omega_0$. This is in contrast to the results of two decades of intense studies [1] of current pumping in spintronics by dynamical magnetization where only spin current $I_p^{S_z}$ is found, with one of its three components being DC and the other two oscillating with frequency ω_0. We additionally employ the Floquet NEGF formalism, combining the Floquet scattering matrix [29] with time-independent NEGF calculations [21], which allows us to precisely estimate (figures 4 and 5) the cutoff harmonic $N_{\max}$ as well as validate the TDNEGF calculations (that are initially deployed to unearth any

[1] See Supplementary data for a movie and its accompanying text, which consist of a movie animating time-dependence of nonequilibrium electronic spin density, as well as a file explaining details of the movie. The movie animates time-dependence of nonequilibrium spin density, $\langle \hat{\mathbf{s}}_1 \rangle^{\text{neq}}(t)$ at site 1 in the FM case (figure 1(a)), for different values of the Rashba SO coupling $\gamma_{SO} \in \{0, 0.4\gamma, 1.0\gamma\}$, together with time-dependence of the classical localized magnetic moment $\mathbf{M}_1(t)$ steadily precessing with precession cone angle θ and frequency ω_0. The time-dependence and the corresponding FFT of the Cartesian components of $\langle \hat{\mathbf{s}}_1 \rangle^{\text{neq}} \equiv (\langle \hat{s}_1^x \rangle^{\text{neq}}, \langle s_1^y \rangle^{\text{neq}}, \langle s_1^z \rangle^{\text{neq}})$ is provided in the file.

processes beyond Floquet-based formalism, such as non-integer harmonics). Our prescription for experimental realization of this effect is based (figures 1(c) and 5) on 2D FM or AFM materials [36, 37, 56], which have intrinsically strong SOC that can be easily further tailored by the proximity effect [62] to nonmagnetic 2D materials [65] within van der Waals heterostructures. Finally, for AF materials driven into resonance by ω_0 in the sub-THz range [8, 9], the $I_p(t)$ they pump would generate output THz radiation at multiples of the driving frequency ω_0, thereby opening new avenues for THz spintronics where such output radiation is currently generated by more complex F [67] or AF heterostructures [68, 69] driven by femtosecond laser pulses.

5. Note added

Recently, we became aware of work [70] in which high harmonics in only charge current pumped by a AFM (defined on the square lattice including Rashba SOC) were studied using a different type of TDNEGF code than the one employed by us (in figures 2 and 3). However, computed pumped current versus time in [70] violates 'two general theorems' of time-dependent quantum transport as soon as SOC is switched on (as discussed in more detail in [71]). Also, comparison of figures 3 and 4 shows that it is virtually impossible to extract the precise value of $N_{\max}$ solely from FFT of TDNEGF calculations (figure 3), i.e. without involving some type of Floquet NEGF algorithm, such as the one developed in our study (equations (5)–(12)).

Data availability statement

All data that support the findings of this study are included within the article (and any supplementary files).

Acknowledgments

This work was supported by the US National Science Foundation (NSF) through the University of Delaware Materials Research Science and Engineering Center DMR-2011824.

ORCID iDs

Jalil Varela-Manjarres https://orcid.org/0000-0003-3823-4147
Branislav K Nikolić https://orcid.org/0000-0002-5793-7764

References

[1] Tserkovnyak Y, Brataas A, Bauer G E W and Halperin B I 2005 Nonlocal magnetization dynamics in ferromagnetic heterostructures *Rev. Mod. Phys.* **77** 1375
[2] Ando K 2014 Dynamical generation of spin currents *Semicond. Sci. Technol.* **29** 043002
[3] Fan X, Himbeault E, Gui Y S, Wirthmann A, Williams G, Xue D and Hu C-M 2010 Electrical detection of large cone angle spin precession from the linear to the nonlinear regime *J. Appl. Phys.* **108** 046102
[4] Switkes M, Marcus C M, Campman K and Gossard A C 1999 An adiabatic quantum electron pump *Science* **283** 1905
[5] Brouwer P W 1998 Scattering approach to parametric pumping *Phys. Rev.* B **58** R10135
[6] Bajpai U, Popescu B S, Plecháč P, Nikolić B K, Foa Torres L E F, Ishizuka H and Nagaosa N 2019 Spatio-temporal dynamics of shift current quantum pumping by femtosecond light pulse *J. Phys. Mater.* **2** 025004
[7] Yang F and Hammel P C 2018 FMR-driven spin pumping in $Y_3Fe_5O_{12}$-based structures *J. Phys. D: Appl. Phys.* **51** 253001
[8] Vaidya P, Morley S A, van Tol J, Liu Y, Cheng R, Brataas A, Lederman D and del Barco E 2020 Subterahertz spin pumping from an insulating antiferromagnet *Science* **368** 160
[9] Li J *et al* 2020 Spin current from sub-terahertz-generated antiferromagnetic magnons *Nature* **578** 70
[10] Zhang S and Zhang S S-L 2009 Generalization of the Landau–Lifshitz–Gilbert equation for conducting ferromagnets *Phys. Rev. Lett.* **102** 086601
[11] Weindler T, Bauer H G, Islinger R, Boehm B, Chauleau J-Y and Back C H 2014 Magnetic damping: domain wall dynamics versus local ferromagnetic resonance *Phys. Rev. Lett.* **113** 237204
[12] Petrović M D, Popescu B S, Bajpai U, Plecháč P and Nikolić B K 2018 Spin and charge pumping by a steady or pulse-current-driven magnetic domain wall: a self-consistent multiscale time-dependent quantum-classical hybrid approach *Phys. Rev. Appl.* **10** 054038
[13] Petrović M D, Bajpai U, Plecháč P and Nikolić B K 2021 Annihilation of topological solitons in magnetism with spin wave burst finale: the role of nonequilibrium electrons causing nonlocal damping and spin pumping over ultrabroadband frequency range *Phys. Rev.* B **104** L020407
[14] Abbout A, Weston J, Waintal X and Manchon A 2018 Cooperative charge pumping and enhanced skyrmion mobility *Phys. Rev. Lett.* **121** 257203
[15] Suresh A, Bajpai U and Nikolić B K 2020 Magnon-driven chiral charge and spin pumping and electron-magnon scattering from time-dependent quantum transport combined with classical atomistic spin dynamics *Phys. Rev.* B **101** 214412
[16] Chen S-H, Chang C-R, Xiao J Q and Nikolić B K 2009 Spin and charge pumping in magnetic tunnel junctions with precessing magnetization: a nonequilibrium Green function approach *Phys. Rev.* B **79** 054424
[17] Cheng R, Xiao J, Niu Q and Brataas A 2014 Spin pumping and spin-transfer torques in antiferromagnets *Phys. Rev. Lett.* **113** 057601
[18] Saitoh E, Ueda M, Miyajima H and Tatara G 2006 Conversion of spin current into charge current at room temperature: inverse spin-Hall effect *Appl. Phys. Lett.* **88** 182509

[19] Wei D, Obstbaum M, Ribow M, Back C H and Woltersdorf G 2014 Spin Hall voltages from A.C. and D.C. spin currents *Nat. Commun.* **5** 3768
[20] Jamali M, Lee J S, Jeong J S, Mahfouzi F, Lv Y, Zhao Z, Nikolić B K, Mkhoyan K A, Samarth N and Wang J-P 2015 Giant spin pumping and inverse spin Hall effect in the presence of surface and bulk spin–orbit coupling of topological insulator Bi_2Se_3 *Nano Lett.* **15** 7126
[21] Mahfouzi F, Fabian J, Nagaosa N and Nikolić B K 2012 Charge pumping by magnetization dynamics in magnetic and semimagnetic tunnel junctions with interfacial Rashba or bulk extrinsic spin-orbit coupling *Phys. Rev.* B **85** 054406
[22] Mahfouzi F, Nagaosa N and Nikolić B K 2014 Spin-to-charge conversion in lateral and vertical topological-insulator/ferromagnet heterostructures with microwave-driven precessing magnetization *Phys. Rev.* B **90** 115432
[23] Dolui K, Bajpai U and Nikolić B K 2020 Effective spin-mixing conductance of topological-insulator/ferromagnet and heavy-metal/ferromagnet spin-orbit-coupled interfaces: a first-principles Floquet-nonequilibrium Green function approach *Phys. Rev. Mater.* **4** 121201(R)
[24] Dolui K, Suresh A and Nikolić B K 2022 Spin pumping from antiferromagnetic insulator spin-orbit-proximitized by adjacent heavy metal: a first-principles Floquet-nonequilibrium Green function study *J. Phys. Mater.* **5** 034002
[25] Ahmadi A and Mucciolo E R 2017 Microscopic formulation of dynamical spin injection in ferromagnetic-nonmagnetic heterostructures *Phys. Rev.* B **96** 035420
[26] Chen K and Zhang S 2015 Spin pumping in the presence of spin-orbit coupling *Phys. Rev. Lett.* **114** 126602
[27] Liu Y, Yuan Z, Wesselink R, Starikov A A and Kelly P J 2014 Interface enhancement of Gilbert damping from first principles *Phys. Rev. Lett.* **113** 207202
[28] Arrachea L and Moskalets M 2006 Relation between scattering-matrix and Keldysh formalisms for quantum transport driven by time-periodic fields *Phys. Rev.* B **74** 245322
[29] Moskalets M V 2011 *Scattering Matrix Approach to Non-Stationary Quantum Transport* (Imeprial College Press)
[30] Shevtsov O and Waintal X 2013 Numerical toolkit for electronic quantum transport at finite frequency *Phys. Rev.* B **87** 085304
[31] Schmid C P *et al* 2021 Tunable non-integer high-harmonic generation in a topological insulator *Nature* **593** 385
[32] Lin H-C 2014 Sources, effects and modelling of interharmonics *Math. Probl. Eng.* **2014** 730362
[33] Gaury B, Weston J, Santin M, Houzet M, Groth C and Waintal X 2014 Numerical simulations of time-resolved quantum electronics *Phys. Rep.* **534** 1
[34] Manchon A, Koo H C, Nitta J, Frolov S M and Duine R A 2015 New perspectives for Rashba spin–orbit coupling *Nat. Mater.* **14** 871
[35] Gibertini M, Koperski M, Morpurgo A F and Novoselov K S 2019 Magnetic 2D materials and heterostructures *Nat. Nanotechnol.* **14** 408
[36] Olsen T 2019 Theory and simulations of critical temperatures in CrI_3 and other 2D materials: easy-axis magnetic order and easy-plane Kosterlitz–Thouless transitions *MRS Commun.* **9** 1142
[37] Vanherck J, Bacaksiz C, Sorée B, Milošević M V and Magnus W 2020 2D ferromagnetism at finite temperatures under quantum scrutiny *Appl. Phys. Lett.* **117** 052401
[38] Popescu B S and Croy A 2016 Efficient auxiliary-mode approach for time-dependent nanoelectronics *New J. Phys.* **18** 093044
[39] Nikolić B K, Zârbo L P and Souma S 2006 Imaging mesoscopic spin Hall flow: spatial distribution of local spin currents and spin densities in and out of multiterminal spin-orbit coupled semiconductor nanostructures *Phys. Rev.* B **73** 075303
[40] Cooper R L and Uehling E A 1967 Ferromagnetic resonance and spin diffusion in supermalloy *Phys. Rev.* **164** 662
[41] Stefanucci G and van Leeuwen R 2013 *Nonequilibrium Many-Body Theory of Quantum Systems: A Modern Introduction* (Cambridge University Press)
[42] Shirley J H 1965 Solution of the Schrödinger equation with a Hamiltonian periodic in time *Phys. Rev.* **138** B979
[43] Sambe H 1973 Steady states and quasienergies of a quantum-mechanical system in an oscillating field *Phys. Rev.* A **7** 2203
[44] Eckardt A and Anisimovas E 2015 High-frequency approximation for periodically driven quantum systems from a Floquet-space perspective *New J. Phys.* **17** 093039
[45] Bajpai U, Ku M J H and Nikolić B K 2020 Robustness of quantized transport through edge states of finite length: imaging current density in Floquet topological versus quantum spin and anomalous Hall insulators *Phys. Rev. Res.* **2** 033438
[46] Velev J and Butler W 2004 On the equivalence of different techniques for evaluating the Green function for a semi-infinite system using a localized basis *J. Phys.: Condens. Matter* **16** R637
[47] Kohler S, Lehman J and Hänggi P 2005 Driven quantum transport on the nanoscale *Phys. Rep.* **406** 379
[48] Foa Torres L E F 2005 Mono-parametric quantum charge pumping: interplay between spatial interference and photon-assisted tunneling *Phys. Rev.* B **72** 245339
[49] Fisher D S and Lee P A 1981 Relation between conductivity and transmission matrix *Phys. Rev.* B **23** 6851
[50] Hattori K 2007 Spin pumping from finite-sized electron systems in ballistic and diffusive transport regimes *Phys. Rev.* B **75** 205302
[51] Tatara G 2016 Green's function representation of spin pumping effect *Phys. Rev.* B **94** 224412
[52] Tatara G 2019 Effective gauge field theory of spintronics *Physica* E **106** 208
[53] Bajpai U and Nikolić B K 2020 Spintronics meets nonadiabatic molecular dynamics: geometric spin torque and damping on dynamical classical magnetic texture due to an electronic open quantum system *Phys. Rev. Lett.* **125** 187202
[54] Vavilov M G, Ambegaokar V and Aleiner I L 2001 Charge pumping and photovoltaic effect in open quantum dots *Phys. Rev.* B **63** 195313
[55] Costache M V, Watts S M, van der Wal C H and van Wees B J 2008 Electrical detection of spin pumping: DC voltage generated by ferromagnetic resonance at ferromagnet/nonmagnet contact *Phys. Rev.* B **78** 064423
[56] Ghimire S and Reis D A 2019 High-harmonic generation from solids *Nat. Phys.* **15** 10
[57] Bai Y, Fei F, Wang S, Li N, Li X, Song F, Li R, Xu Z and Liu P 2021 High-harmonic generation from topological surface states *Nat. Phys.* **17** 311
[58] Ikeda T N and Sato M 2019 High-harmonic generation by electric polarization, spin current and magnetization *Phys. Rev.* B **100** 214424
[59] Takayoshi S, Murakami Y and Werner P 2019 High-harmonic generation in quantum spin systems *Phys. Rev.* B **99** 184303
[60] Tancogne-Dejean N, Eich F G and Rubio A 2022 Effect of spin-orbit coupling on the high harmonics from the topological Dirac semimetal Na_3Bi *npj Comput. Mater.* **8** 145
[61] Lysne M, Murakami Y, Schüler M and Werner P 2020 High-harmonic generation in spin-orbit coupled systems *Phys. Rev.* B **102** 081121(R)
[62] Žutić I, Matos-Abiague A, Scharf B, Dery H and Belashchenko K 2019 Proximitized materials *Mater. Today* **22** 85

[63] Marmolejo-Tejada J M, Dolui K, Lazić P, Chang P-H, Smidstrup S, Stradi D, Stokbro K and Nikolić B K 2017 Proximity band structure and spin textures on both sides of topological-insulator/ferromagnetic-metal interface and their charge transport probes *Nano Lett.* **17** 5626
[64] Qiu H *et al* 2020 Spin-orbit-proximitized ferromagnetic metal by monolayer transition metal dichalcogenide: atlas of spectral functions, spin textures and spin-orbit torques in Co/$MoSe_2$, Co/WSe_2 and Co/$TaSe_2$ heterostructures *Phys. Rev. Mater.* **4** 104007
[65] Dolui K, Petrović M D, Zollner K, Plecháč P, Fabian J and Nikolić B K 2020 Proximity spin-orbit torque on a two-dimensional magnet within van der Waals heterostructure: current-driven antiferromagnet-to-ferromagnet reversible nonequilibrium phase transition in bilayer CrI_3 *Nano Lett.* **20** 2288
[66] Ciccarelli C, Hals K M D, Irvine A, Novak V, Tserkovnyak Y, Kurebayashi H, Brataas A and Ferguson A 2015 Magnonic charge pumping via spin–orbit coupling *Nat. Nanotechnol.* **10** 50
[67] Seifert T *et al* 2016 Efficient metallic spintronic emitters of ultrabroadband terahertz radiation *Nat. Photon.* **10** 483
[68] Ciccarelli C, Hals K M D, Irvine A, Novak V, Tserkovnyak Y, Kurebayashi H, Brataas A and Ferguson A 2021 Ultrafast spin current generated from an antiferromagnet *Nat. Phys.* **17** 388
[69] Suresh A and Nikolić B K 2023 Quantum classical approach to spin and charge pumping and the ensuing radiation in terahertz spintronics: example of the ultrafast light-driven Weyl antiferromagnet Mn_3Sn *Phys. Rev.* B **107** 174421
[70] Ly O and Manchon A 2022 Spin-orbit coupling induced ultrahigh-harmonic generation from magnetic dynamics *Phys. Rev.* B **105** L180415
[71] Nikolić B K and Varela-Manjarres J 2022 Comment on 'Spin-orbit coupling induced ultrahigh-harmonic generation from magnetic dynamic' with prescriptions on how to validate scientific software for computational quantum transport (arXiv:2212.06895)

Supplementary Data for "High-harmonic generation in spin and charge current pumping at ferromagnetic or antiferromagnetic resonance in the presence of spin-orbit coupling"

Jalil Varela-Manjarres and Branislav K. Nikolić*
Department of Physics and Astronomy, University of Delaware, Newark, DE 19716, USA

This Supplementary Data consist of a movie `noneq_spin_density.mp4` and this text guiding the reader on how to watch and interpret the movie. The movie animates time-dependence of nonequilibrium spin density

$$\langle \hat{\mathbf{s}}_1 \rangle^{\rm neq}(t) = {\rm Tr}\left[|1\rangle\langle 1| \otimes \hat{\boldsymbol{\sigma}} \boldsymbol{\rho}^{\rm neq}(t)\right], \tag{1}$$

on site 1 in the ferromagnetic metal (FM) case [Fig. 1(a) in the main text], for different values of the Rashba SO coupling $\gamma_{\rm SO} \in \{0, 0.4\gamma, 1.0\gamma\}$ [Eq. (1) in the main text]. It also animates $\mathbf{M}_1(t)$, steadily precessing with precession cone angle $\theta = 20^\circ$ and frequency $\hbar\omega_0 = 0.01$ eV employed in the main text, whose time-dependence drives conduction electron out of equilibrium to generate $\langle \hat{\mathbf{s}}_1 \rangle^{\rm neq}(t)$. In Eq. (1), $|1\rangle$ is localized orbital on site 1 of one-dimensional (1D) tight-binding chain; $\boldsymbol{\rho}^{\rm neq}(t)$ is time-dependent nonequilibrium density matrix obtained from Eq. (2) in the main text using time-dependent nonequilibrium Green's functions; and $\hat{\boldsymbol{\sigma}} = (\hat{\sigma}_x, \hat{\sigma}_y, \hat{\sigma}_z)$ is the vector of the Pauli matrices.

The time-dependence and the corresponding fast Fourier transform (FFT) of the Cartesian components of $\langle \hat{\mathbf{s}}_1 \rangle^{\rm neq} \equiv (\langle \hat{s}_1^x \rangle^{\rm neq}, \langle s_1^y \rangle^{\rm neq}, \langle s_1^z \rangle^{\rm neq})$ are shown in Figs. S1(a)–(c) and Figs. S1(d)–(f), respectively. In the case without SO coupling ($\gamma_{\rm SO} = 0$ in the movie and in Fig. S1), time-dependence of $\langle \hat{\mathbf{s}}_1 \rangle^{\rm neq}(t)$ provides rigorous backing of a physical picture (see, e.g., Fig. 2 in Ref. [1]) where precessing magnetization of FM layer pumps into adjacent normal metal layer spin current comprised of flowing and precessing electronic spins. That is, in this case flowing $\langle \hat{s}_1^z \rangle^{\rm neq}$ is

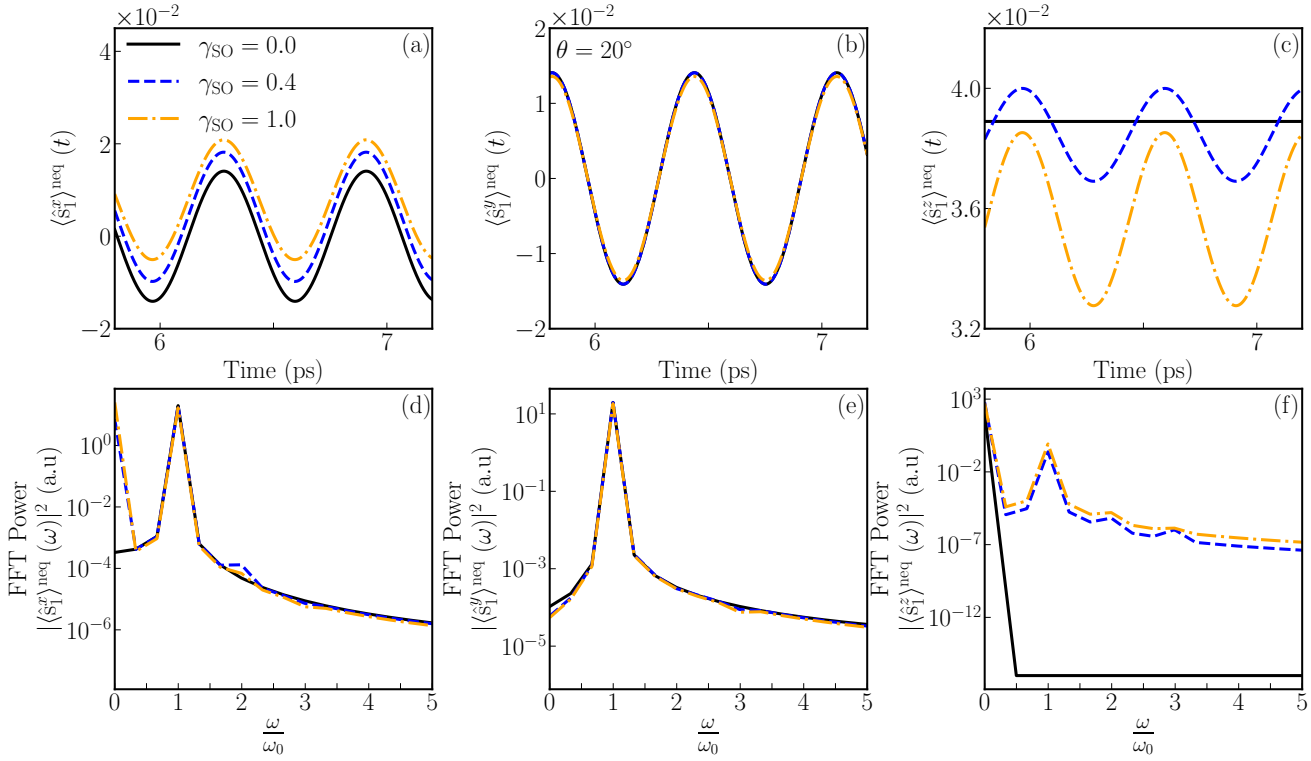

FIG. S1. (a)–(c) Time-dependence of the Cartesian components of $\langle \hat{\mathbf{s}}_1 \rangle^{\rm neq}$ on site 1 of FM [Fig. 1(a) in the main text] whose classical localized magnetic moments $\mathbf{M}_i(t)$ are parallel and steadily precessing with precession cone angle $\theta = 20^\circ$ and frequency $\hbar\omega_0 = 0.01$ eV. Panels (d)–(f) plot FFT of time-dependences in the respective panels (a)–(c).

* bnikolic@udel.edu

time-independent, so that the corresponding component of spin current vector I_z^S is also time independent as found in the "standard model" [2]. However, once the Rashba SO coupling is turned on ($\gamma_{\rm SO} \neq 0$ in the movie and in Fig. S1), $\langle \hat{s}_1^z \rangle^{\rm neq}(t)$ starts to nutate at ω_0 and its multiples [Figs. S1(c) and Figs. S1(f)], which then also leads to time-dependent $I_z^S(t)$ [Fig. 2 in the main text] exhibiting high harmonics [Figs. 2(c) and 3(a) in the main text]. In the movie, time-dependence in Fig. S1(c) is animated by changing the inner color of each of the three arrows representing $\langle \hat{\mathbf{s}}_1 \rangle^{\rm neq}(t)$ for different values of $\gamma_{\rm SO}$.

The movie also reveals that even though $\mathbf{M}_i(t)$ precesses on much slower time scale than the characteristic time scale for electron spin dynamics, $\langle \hat{\mathbf{s}}_i \rangle^{\rm neq}$ is always somewhat behind the 'adiabatic direction', i.e., behind $\mathbf{M}_i(t)$. That such *nonadiabaticity* of electron spin dynamics—where electron spin under time-dependent external field *does not* remain in the lowest energy state at each time and nonadiabatic component $\langle \hat{\mathbf{s}}_i \rangle^{\rm neq} \propto \mathbf{M}_i \times d\mathbf{M}_i/dt$ of nonequilibrium spin density is, therefore, generated—is essential for spin pumping effect has been discussed before [3] (see insightful Sec. 7.2 and Figs. 18 and 19 of Ref. [3]). Furthermore, our movie demonstrates how turning on and then increasing SO coupling enhances the time lag between $\langle \hat{\mathbf{s}}_i \rangle^{\rm neq}(t)$ and $\mathbf{M}_i(t)$. Nevertheless, the pumped current remains adiabatic in the sense (current $\propto \omega_0$) of general (i.e., with or without spins being pumped) quantum pumping theory [4–7].

[1] M. V. Costache, S. M. Watts, C. H. van der Wal, and B. J. van Wees, Electrical detection of spin pumping: dc voltage generated by ferromagnetic resonance at ferromagnet/nonmagnet contact, Phys. Rev. B **78**, 064423 (2008).

[2] Y. Tserkovnyak, A. Brataas, G. E. W. Bauer, and B. I. Halperin, Nonlocal magnetization dynamics in ferromagnetic heterostructures, Rev. Mod. Phys. **77**, 1375 (2005).

[3] G. Tatara, Effective gauge field theory of spintronics, Physica E **106**, 208 (2019).

[4] P. W. Brouwer, Scattering approach to parametric pumping, Phys. Rev. B **58**, R10135 (1998).

[5] M. G. Vavilov, V. Ambegaokar, and I. L. Aleiner, Charge pumping and photovoltaic effect in open quantum dots, Phys. Rev. B **63**, 195313 (2001).

[6] L. E. F. Foa Torres, Mono-parametric quantum charge pumping: Interplay between spatial interference and photon-assisted tunneling, Phys. Rev. B **72**, 245339 (2005).

[7] U. Bajpai, B. S. Popescu, P. Plecháč, B. K. Nikolić, L. E. F. Foa Torres, H. Ishizuka, and N. Nagaosa, Spatio-temporal dynamics of shift current quantum pumping by femtosecond light pulse, J. Phys.: Mater. **2**, 025004 (2019).